River ice controls permafrost bank erosion across an Arctic delta

Abstract

Bank erosion in Arctic rivers helps shape channel geometry, mobilizes carbon from permafrost, and influences sediment delivery to the Arctic Ocean. On Alaska's Arctic coastal plain, rivers begin flowing during snowmelt in late spring while extensive river ice persists in channels, such that hydraulics are altered and water is kept cool. The effects of river ice on permafrost bank erosion are poorly understood, primarily due to a dearth of field observations and a lack of river ice in existing models.

To address this knowledge gap, we developed a numerical model to simulate melt of substrate interstitial ice and bank collapse along individual permafrost river banks. We parameterize the model with field observations from riverbanks in three different channels on the Canning River delta which are disparately impacted by river ice during snowmelt. We explore the bank erosion produced without river ice in the model and with modern river ice model scenarios that we drive with different stage and water temperature boundary conditions. We also compare predicted erosion rates to observations from satellite imagery to validate this approach.

In the model, banks are idealized as vertical profiles that rise 1-2 m above the river bed and are comprised of silt- to sand-sized sediment with dense roots in the active layer. Underneath, we generalize bank ice content underneath the active layer to represent ice-rich permafrost on the river corridor boundaries. The model predicts that these ice-rich river banks can erode by 2-6 m/yr. Scenarios without ice underpredict erosion in the distributary channels. Scenarios with varying river ice for different deltaic channels produce erosion rates similar to observations.

Our results suggest that the prolonged melt of thick river ice in a delta nonlinearly impacts permafrost bank erosion by blocking river discharge to certain branches, heightening stage across the distributary network and locally limiting river water warming. Given expected changes in air temperature and hydrology, future estimates of Arctic river bank erosion could be improved by considering river ice.

Keywords: thermal erosion, icing, permafrost, river bank erosion, Arctic river, bank collapse, ablation,

1. INTRODUCTION

Warming in the Arctic is destabilizing permafrost landscapes (Lachenbruch and Marshall, 1986; Biskaborn et al., 2019). Permafrost is ground that remains at or below 0°C for at least 2 years (Harris et al., 1988). Climate reanalysis suggests that near-surface air temperature in the Arctic rose by 2.7 °C between 1971 and 2017, much faster than global warming trends (Box et al., 2019). Rising surface temperatures have warmed shallow subsurfaces by approximately 0.5 °C per decade and thawed previously perennially frozen ground (Biskaborn et al., 2019, Lachenbruch and Marshall, 1986; Romanovsky, Smith and Christiansen, 2010; Smith et al., 2022).

Permafrost also warms and thaws from surface water interactions (Kokelj and Jorgenson, 2013; Turetsky et al., 2020; Tananaev and Lotsari, 2022). Arctic rivers can rapidly erode ice-rich permafrost river banks when heat transferred by river water supplies the energy required to melt interstitial ice, allowing the substrate to be entrained as the ice cement is removed (Chassiot, Lajeunesse and Bernier, 2020; Tananaev and Lotsari, 2022). This process, termed 'thermal erosion', undercuts banks and generates overhanging blocks that episodically collapse (Walker and Hudson, 2003; Douglas, Dunne and Lamb, 2023). Together, thermal erosion and upper bank collapse result in lateral bank erosion. Additional geomorphic work is done by abrasion of banks floating ice (Ettema, 2002), but the importance of this process is more limited for ice-rich permafrost banks with noncohesive soils that are typical of the coastal lowlands in the North Slope of Alaska.

Permafrost river banks laterally erode by 1–10 m/yr, which is nine times slower than selected lower-latitude river systems for comparison (Rowland et al., 2023). Rates as high as 40 m in a year are reported in the Lena River in Russia (Costard et al., 2014) but are less than 6 m/yr on the Koyukuk River in Interior Alaska (Geyman et al., 2024). We lack data from smaller, mountain-front systems that better represent rivers in the Arctic Coastal Plain.

Dominant controls on thermal erosion in Arctic river corridors vary between systems, but the existence of interstitial pore ice in floodplain soils always relevant. When volumetric ice content exceeds 40%, erosion rates are especially sensitive to water temperature because the latent heat in river bank material is low (Dupeyrat et al., 2011). Additionally, sediment below this threshold ice content is less likely to collapse upon thaw than ice-cemented sediment and might not be entrained as fast as ablation frees sediment (Douglas and Lamb, 2024).

Permafrost exposure to river water is also a primary control on thermal erosion. Tananaev (2016) assessed the thermal erosion of river banks on

the Lena River and report a correspondence between thermal erosion and bank exposure to river water at high stages, suggesting that exposure to water of any temperature controls erosion. Therefore, thermal erosion of river banks will generally be sensitive to inundation, water temperature, and the material properties of frozen ground.

Globally, land surfaces are projected to warm another 1.5°C this century (IPCC, 2023) and permafrost will continue warming at depth (Biskaborn et al., 2019). Based on climate reanalysis, Alaskan river water discharge in Spring is rising by 15% per decade, and discharge in the cold season is rising by 10% per decade (Blaskey et al., 2023). Models suggest that river bank thermal erosion rates could rise from higher net fluvial heat fluxes and an increased capacity to remove collapsed sediment (Douglas, Dunne and Lamb, 2023; Rowland et al., 2023; Fields et al., 2025). However, Ielpi et al. (2023) reports a decline in erosion rates along large meandering permafrost rivers, hypothesizing that vegetation encroachment stabilizes river banks.

River ice may also influence rates of bank erosion in Arctic rivers (Ettema, 2002). River ice can occupy river corridors for six to nine months of the year (Turcotte and Morse, 2013; Yang, Pavelsky, and Allen, 2020; Koch, Connolly, et al., 2024). On deltas in the Arctic National Wildlife Refuge in northern Alaska, and elsewhere in the Arctic, smaller patches of especially persistent river ice, called "icings" can fill the active channel and last all year (Ensom et al., 2020; Yang, Pavelsky, and Allen, 2020; Koch, Best, et al., 2024).

Thermal and mechanical processes gradually clear channels of ice over a river ice break-up period (Turcotte and Morse, 2013). Initially, thermal break-up' ensues as ice gradually melts in place until it can no longer resist downstream motion and flows downstream, termed 'mechanical break-up' (Burrell et al., 2023; Prowse and Beltaos, 2002). The river ice break-up period in the Arctic starts in late spring (May-June) and is often associated with annual peak water discharge (Walker and Hudson, 2003).

Icings cause flooding during the break-up period. River ice can promote flooding during snowmelt by changing channel geometry and flow pathways (Prowse and Beltaos, 2002; Best, Mcnamara, and Liberty, 2005; Wohl and Scamardo, 2022). River ice also cools water during the thermal break-up period. Although persistent river ice can keep water temperatures near 0°C for weeks (Marsh and Prowse, 1987), near-freezing water still transfers heat and can slowly thaw frozen ground (Randriamazaoro et al., 2007; Dupeyrat et al., 2011). Previous models for bank erosion do not model ice impacts on channel geometry nor water temperature (Costard et al., 2003; Douglas, Dunne and Lamb, 2023) and are therefore limited in their ability to model erosion during the break-up period.

With continued surface warming and hydrologic change, river ice conditions during snowmelt are in flux (Prowse and Beltaos, 2002; Box et al., 2019; Burrell, Beltaos, and Turcotte, 2023). River ice development begins later and snowmelt starts earlier, leading to 6.1 more ice-free days per 1°C increase in mean annual air temperature (Magnuson et al., 2000; Yang, Pavelsky, and Allen, 2020). Few studies explore how unprecedented river ice conditions during snowmelt could limit or enhance permafrost bank erosion (Kane et al., 2000; Overeem, Nienhuis and Piliouras, 2022).

On Arctic deltas, the trajectory of permafrost bank erosion is clouded by the potential for unusually thick or thin river ice conditions during snowmelt. We investigate how the duration of thermal break-up impacts permafrost bank erosion rates in a delta. We model bank erosion rates based on field observations from the Canning River delta in northern Alaska, USA. We drive the model with environmental conditions derived from in-situ monitoring of hydrology and meteorology. To evaluate our approach, we compare modelled bank erosion rates to measurements acquired from remote-sensing data.

2. STUDY SITE

The Canning River is in the Arctic National Wildlife Refuge, Alaska, USA. It drains 5,000 km^2 upstream of the delta apex and an additional 80 km^2 on the coastal plain, all of which is in continuous permafrost terrain (Figure 1). In its headwaters in the Brooks Range, the Canning River incises limestone and other Devonian and Carboniferous sedimentary bedrock Wilson et al., 2015. Ice occupied valleys in the Brooks Range and the Sadlerochit Mountains in the Pleistocene (Briner and Kaufman, 2008). These valleys are now home to braided to anastomosing gravel-bedded rivers. Downstream and approximately 32 km from the coast, the Canning River crosses a subtle morainal ridge, the postulated farthest late-Pleistocene glacial extent (Briner and Kaufman, 2008). At this location, near the Staines airstrip, the river corridor narrows before bifurcating into multiple distributary channels that ultimately drain into the Beaufort Sea. Because the Beaufort Sea is microtidal, delta channels are minimally impacted by salt water and backwater.

The Canning River's annual hydrograph is dominated by a peak annual flood called snowmelt (Figure 2A). This region of Alaska receives about 182 to 219 mm of precipitation annually (Xie and Arkin, 1997). Mean annual air temperature on the coastal plain is -8°C; monthly mean air temperature ranges from -35 to 10°C (Figure 2A; N69.87416°, W146.17744°, Frank Urban, Canning River Meteorological Station, unpublished data, 2023). When air temperature rises above freezing, around May 15th, runoff from snowmelt drains through the Canning River and its distributary channels (Figure 1C). In 2009, a peak flow of 926 m^3/s was measured in the Canning River at the

U.S. Geological Survey stream gauge at Staines (Figure 2B; U.S. Geological Survey, 2023). During summer storms, peak flows at this gauge of 680 m^3/s at a 0.02% annual exceedance probability occurred (Figure 2B, Koch, Best, et al., 2024).

About 40 km upstream from the coast, the river forms a delta apex and splits into three active distributary channels: the Staines River (westmost), the Canning River (eastmost), and the West Canning River (in between) (Figure 1, E). An extensive icing covers the reach of the West Canning River between the delta apex and the Staines River and influences water partitioning between all three rivers each year. The Staines River is completely covered by ice in spring and appears to receive most discharge from the delta apex in summer (Figure 1B-D). The Canning River is not blocked by ice and receives most of its discharge in spring and less discharge in summer (Figure 1B-D). The West Canning River can be blocked by the icing during snowmelt and only receives flow in spring (Figure 1B-D). The relative amounts of blockage vary from year to year.

The distributary channels flow across the Arctic coastal plain that is characterized by ice-rich permafrost, with ice wedge polygonal tundra (Kanevskiy, Shur and Jorgenson, 2018). These channels impinge on frozen ground at the edges of the river corridor, where river water can inundate river banks at high flow. River banks on the edges of the river corridor can be several meters high and are rich in millennial-aged carbon-rich soils (Anderson et al., 2024). Within the river corridor, vegetated surfaces have been augmented by fluvial processes and are less likely to be underlain by frozen ground.

We focus on the Canning River in its distributary channel network on the delta where it is in contact with the river corridor boundary near our field survey sites – the eastern bank at the delta apex, the western river bank in the Staines River distributary channel, downstream of the icing, and the eastern river bank in the Canning River distributary channel (Figure 1E). Here, the river corridor boundaries retreat from thermal erosion and bank collapse.

3. METHODS

We assess how the river icing in the Canning River delta affects river bank erosion of permafrost at the river corridor boundaries. We describe field observations and our numerical model of bank erosion that includes heat transfer, hydrodynamics, and river ice. Lastly, we detail how remote sensing measurements were made.

3.1 Field Surveys

We collected field data during repeat surveys conducted between 2021 and 2024. Each survey site occupied a unique hydrologic setting: the delta apex and the two most frequently occupied distributary channels – the Staines and Canning Rivers. At each site, we made measurements along vertical profiles at representative river banks.

We manually measured bank morphology, including bank height, surface slopes, and horizontal distance between slope breaks. We made these measurements with a measuring tape and level.

We collected thaw depth data along the same profiles using a ThermoWorks temperature probe, noting vertical temperature profiles and thaw depth or depth to refusal. These soil and substrate temperature data were collected at regular spacing over a 25 – 50 m transect along the top surface of the bank. We also measured temperature and distance to refusal along the vertical bank exposure.

We collected sediment samples from representative layers exposed along the vertical profiles to characterize their grain size distribution (GSD). We processed sediment samples at the sedimentology laboratory Institute of the Arctic and Alpine Research (INSTAAR) at the University of Colorado Boulder. Between collection and processing, samples were kept in a freezer at -5°C to avoid loss of moisture content during storage. We measured the volumetric water and ice content of the bank material as the gravimetric water content corrected for the measured weight of sample. We measured the GSD via laser diffraction particle size analysis on a Malvern Panalytical, Inc. (Westborough, Massachusetts, USA) Mastersizer 3000. We removed organic matter with hydrogen peroxide treatment and sieved clasts larger than 4 mm prior to GSD analysis. We approximated the median grain size diameter, D50, of the entire river bank substrate as the average of the 50^{th} percentile grain size of each sampled layer, weighted by layer thickness (Figure S1).

To measure the grain size distribution of fluvial gravel, we performed Wolman Pebble Counts on representative gravel bars and on bank toes, measuring approximately 100 clasts in each count (Wolman, 1954; Bunte and Abt, 2001). We also measured the three-dimensional geometry of collapsed bank blocks to fully characterize bank morphology.

3.2 Channel Transects

We characterized the cross-sectional geometry of the river corridor at each survey site by sampling a digital elevation model (DEM). Along transects drawn perpendicular to the surveyed river bank, we extracted surface elevation from the Arctic Digital Elevation Model (ArcticDEM) mosaic version 4.1 (Porter et al. 2023, Figure S2). ArcticDEM pixel values report the mean elevation from photogrammetry based on satellite imagery collected between 2007 to 2022, at 2 m by 2 m resolution.

We measured channel bankfull dimensions along the transects. We defined a bankfull elevation as the surface elevation on either the left or right river bank – whichever is smaller. We calculated the bankfull channel area by integrating the area between the bankfull elevation and the transect surface elevation along the length between the left and right river banks (Figure S2; Figure S3). We calculated the channel width as the wetted perimeter when the channel is full, and bankfull area divided by bankfull water depth.

3.3 Numerical Modeling

3.3.1 Permafrost Bank Erosion Model

Permafrost banks with ice-rich bank material erode at their base from ablation and subsequent rotational collapse of upper banks (Costard et al., 2003; Barnhart et al., 2014). We simulate ablation of inundated portions of a bank profile by flowing river water and assume that the river immediately entrains all collapsed relatively fine sediment as previously applied to river banks in the Lena River delta (Costard et al. 2003, Dupeyrat et al., 2011). We also account for episodic upper bank collapse with a torque-based collapse criterion following Barnhart et al. (2014), previously applied to coastal permafrost bluff erosion (Hoque and Pollard, 2016; Ravens and Peterson, 2021).

For each survey site in each simulation, we simulate erosion from ablation and collapse along a synthetic bank profile for a duration of $N = 50$ years (Figure S4). A synthetic bank profile is a vertical line discretized at a spacing of $dz = 10$ cm, from $z = 0$ m at the base of a bank to a set bank height, h_b. Ablation is limited to the inundated portion of the bank profile, where river water height relative to the channel bed elevation is denoted by H (m). We calculate the mass and geometry of the overhanging portion of the bank profile after moving the x-coordinate of the inundated portion of the bank by $V_a dt$, where V_a is ablation velocity in m/s and dt is the timestep in seconds. If the collapse criteria is reached, the block is removed from the profile by updating the c-coordinate again.

After each simulation, we use a first order finite difference scheme to approximate a depth-averaged bank erosion rate from the two processes. We calculate a mean annual lateral erosion rate, E (m/yr), as

$$E = \frac{1}{N h_b} \int \int_{z=z_0}^{h_b} \frac{dx}{dt} dz dt \qquad (1)$$

Where N is the number of years in the simulation. E is a time-averaged lateral bank erosion rate. We also calculate a relative erosion rate, E^*,

$$E^* = \frac{E}{W} \qquad (2)$$

Where s (s) is the number of seconds in a year. We use E^* to compare annual erosion rates based on bankfull channel size. We choose bankfull width, W (m), to represent channel size as W varies more between channels than water depth at flood stage.

3.3.1.1 Ablation

We calculate V_a following Costard et al. (2003) as

$$V_a = \frac{C_h (T_w - T_0)}{L_i f_i \rho_i + \rho_s c_p (T_o - T_p)} \qquad (3)$$

where C_h is a fluvial heat transfer coefficient with units of m/s. $(T_w - T_0)$ is the temperature difference between river water and its freezing temperature, in °C. L_i (J/kg) is the latent heat of ice, f_i is the volumetric fraction of ice in permafrost substrate, and ρ_i is the density of ice in kg/m^3. ρ_s is the permafrost bulk density, c_p (J /kg /°C) is the heat capacity of permafrost, and $(T_0 - T_p)$ is the temperature difference between permafrost and the melting temperature of ice. The numerator of (3) describes the fluvial heat flux into the bank, and the denominator describes the energy required both to raise the temperature of bank material to 0°C and to melt interstitial ice (Costard et al., 2003). Model parameters are illustrated in Figure 6 and Figure S4.

We use a function for C_h that applies to non-cohesive river banks with high ice content and easily entrained bank sediment (Dupeyrat et al., 2011). Similar approaches have been applied to pure ice walls and permafrost river banks in the Lena River (Costard et al., 2003; Dupeyrat et al., 2011).

$$C_h = \frac{0.00249 k_w Pr^{1/3} Re^{1.0552}}{H} \qquad (4)$$

Where Re is the flow Reynolds number and is defined as $\frac{UH}{\nu_w}$. Pr is the flow Prandtl number, equal to $\frac{\mu c_{p,w}}{k_w}$. ν_w (m^2 /s) is the kinematic viscosity of river water, $c_{p,w}$ (J /kg /°C) is river water heat capacity, and ρ_w is river water density (kg/m^3). We use the Chézy friction factor, C_f, and shear velocity, U^* $= \sqrt{gHS}$, to define mean flow velocity in turbulent flow, U (m/s),

$$U = \frac{U^*}{\sqrt{C_f}} \qquad (5)$$

$$\sqrt{C_f} = \frac{1}{8.1} \left(\frac{H}{d}\right)^{-\frac{1}{6}} \qquad (6)$$

The bank roughness length scale, d (m), is set equal to 2 times $D84_{bed}$ (Ferguson, 2007, Parker, 1991), as applicable to mixed-grain size gravel-bedded rivers with small sand fractions.

3.3.1.2 Bank Collapse

The upper, overhanging part of a bank can collapse when it reaches a critical mass and geometry relative to resistance from the frozen substrate and roots in the active layer. We model this process with a torque balance. We assume that upper bank resistance to collapse is controlled by the pivot point's distance from the centers of ice wedges at troughs in the floodplain (Barnhart et al., 2013, Hoque and Pollard, 2016). Troughs between polygons on the floodplain surface are located at the centers of ice wedges. The repeated contraction and expansion along this face creates a weak plane (Hoque and Pollard, 2016).

When the driving torque, T_D (J/m), exceeds a resisting torque from permafrost, T_R (J/m), we remove the overhanging portion of the bank above a pivot point from the bank profile along a vertical failure plane (refer to Figure 6 and Figure S4 for model definitions).

$$T_D = \int_{z=z_o}^{z=h_b} \rho_{pf} g [x_o - x(z)]^2 dz \qquad (7)$$

$$T_{pf} = \int_{z=x_o}^{z=x_{iw}} \tau_{pf} [x_o - x(z)][x_{iw} - x_o] dz \qquad (8)$$

$$T_{iw} = \tau_{iw} d_{iw} [x_{iw} - x_o] \qquad (9)$$

$$T_R = \rho_{pf} g [h_b - z_o][x_{iw} - x_o]^2 + T_{pf} + T_{iw} \qquad (10)$$

Here, z_o is the vertical position of the pivot point and x_o is its horizontal pivot point position. We identify the pivot point as the point on the bank profile closest to x_{iw}, the horizontal position of the nearest trough. When $T_D/T_R > 1$, $x_o - x$ is removed from points on the profile above the pivot point. T_R is set by the weight of soil between the bank and ice wedge center, in addition to the tensile strength of permafrost and the ice wedge. The ice wedges are d_{iw} deep, and their centers are placed regularly at a distance Δx_w. In banks with well-developed ice wedges, we set d_{iw} equal to h_b. In banks where ice wedges are minimally developed, we set d_{iw} equal to the depth to refusal observed on the bank surface, and Δx_w equal to 1 m. τ_{pf} (Pa) is the permafrost tensile strength, and τ_{iw} is ice tensile strength, both in Pa (Barnhart et al., 2013, Table 1).

3.3.2 Hydraulic Dynamics

Discharge dictates the water level at which the banks are inundated and river water heat balance. We drive our model with 2009 data, the most complete record. We assume 2009 discharge recorded at U.S. Geological Survey (USGS) streamgage (USGS station 15955000; U.S. Geological Survey, 2023) is representative of the delta apex reach only a few kilometers downstream because the contribution from small tributary inflows between the monitoring and study locations is negligible. The Staines River distributary channel receives a proportion of the discharge flowing from the

delta apex, Q_a, proportional the area not blocked by ice. The Canning River distributary channel receives the remainder of discharge from the delta apex that is not directed to the Staines River distributary channel. Thus, we define discharge in the distributary channels as

$$Q_s = Q_a \left(1 - \frac{A_i}{A_{bf}}\right) \quad (11) \qquad Q_c = Q_a - Q_s \quad (12)$$

where. Q_s (m^3/s) is discharge in the Staines River distributary channel, and Q_c is discharge at the Canning River distributary channel. For our numerical experiments, we ignore small amounts of flow directed into the West Canning River distributary channel, even if they are occasionally occupied as evidenced from the remote-sensing imagery analysis. This is warranted because the exact flow distribution between channels is only known from a few field observations in 2022 and may be variable from year to year.

We predict river water depth based on an existing model for water height during floods when ice occupies channels (Prowse and Beltaos, 2002). To simplify, we assume that the wetted perimeter during flood stages is equal to the bankfull width we measured from satellite data. The model accounts for hydraulically rough flow beneath an ice cover in addition to a layer of submerged, floating ice:

$$H = 1.32\left(\frac{Qn_c}{1.49W\sqrt{S}}\right)^{\frac{3}{5}} + \frac{\rho_i A_i}{W\rho_w} \quad (13)$$

where W (m) is the wetted perimeter at bankfull flood stage, Q (m) is river water discharge, and n_c is the composite manning's roughness coefficient. We set n_c equal to 0.05, as recommended for gravel to cobble-bedded braided rivers with low floodplain vegetation and slump blocks on banks (Coon, 1998).

This approach requires three main assumptions. Equation (13) assumes that channel cross sections are rectangular, which is supported by the high width-to-depth ratios we observe. By maintaining constant n_c values between ice-free and persistent ice scenarios, we also assume that river ice only impacts water surface elevation by removing channel area and does not alter bed resistance to flow. We also assume that stage height cannot exceed the river bank height, h_b, thereby avoiding unrealistic stage increases when water overtops banks.

To compare results based on inundation, we define a metric

$$H^* = \frac{1}{Ns}\int \frac{H}{h_{bf}} dt \quad (14)$$

which quantifies the mean annual height of river bank exposure to river water, relative to the limit set by river banks because river water surface elevation cannot exceed the bankfull elevation (Figure S2).

3.3.3 River Ice

River ice reduces the area available to transmit flow through a cross section. We model cross-sectional channel area occupied by river ice based on an assumed exponential decay of ice volume in time. First, we assume the river ice decays from the channel after a specified start date, t_o (s), over the period τ (s). A_i(m^2), is the channel cross sectional area occupied by ice at a given time, t (s), since January 1st.

$$A_i = A_o e^{-\frac{(t-t_o)}{\tau}} \qquad (15)$$

where A_o (m^2) is the cross-sectional area filled by ice upon the initiation of snowmelt on day t_o (s). We assume A_o to fill a portion of the bankfull channel cross-section. In the Staines River distributary channel occupied by the river icing, we set A_o as A_{bf} (Table 3), where A_{bf} is the bankfull channel wetted area. For the apex reach, ice fills 50% of A_{bf} on t_o. We assume that the Canning River distributary channel has no river ice on t_o. We vary t_o and τ based on surface area reconstructions from satellite data for icings in the Arctic National Wildlife Refuge (Koch, Best, et al., 2024).

We define a metric for the channel area blocked by river ice, A^*,

$$A^* = \frac{1}{Ns}\int \frac{A_i}{A_{bf}} dt \qquad (16)$$

Where A_{bf} (m^2) is the bankfull channel area. We use A^* to compare results based on cumulative ice area relative to the bankfull area.

3.3.4 Water Temperature

Water temperature is a primary control on ablation. To model river water temperature, we apply the heat balance model from Zheng et al. (2019). While ice fills over half the channel, river water temperature, T_w, is set to 0°C. Starting at $t_o + \tau$, when most of the initial river ice cross sectional area has decayed, we begin to solve for T_w. T_w is reset to zero on t_f. We solve for the change in river water heat, ΔHw, based on five different heat fluxes, all in W/m^2:

$$\Delta Hw = Hsr + Hlr + Hl + Hc + Hb \qquad (17)$$

Hsr is the net surface shortwave solar radiation on the river water surface. Hlr is the net surface longwave radiation, such that $Hlr = Hdl - Hel$, where Hdl is atmospheric downward longwave radiation and Hel is emitted longwave elevation. Hl is the latent heat due to evaporation and condensation. Hc is the convective heat flux at the river water surface. Hb is the riverbed heat flux (Webb and Zhang, 1997). Hb is calculated as

$$Hb = -(1-R)His(1-a)(1-b)e^{-fH} - k_b \Delta Tb \qquad (18)$$

Where R is river water surface albedo, His is incident short-wave solar radiation (W/m^2), a is the fraction of radiation absorbed in water, b is the fraction of radiation absorbed by the riverbed, and f is the attenuation coefficient. ΔTb is the thermal gradient at the riverbed. We assume ΔTb is equal to mean annual air temperature divided by a depth to zero temperature change of 30 m below the river bed, or -0.2667 °C/m. this approach has previously been applied to the nearby Kuparuk River – a river of similar substrate and size as the Canning River (Kane et al., 2000; Best et al., 2005) Please refer to Zheng et al. (2019) for further details.

To isolate the impact of river water temperature between model experiments, we use thawing degree-days, TDD (°C days), such that

$$TDD = \frac{365}{Ns}\int (T_w - T_o)dt \qquad (19)$$

3.3.5 Implementation of Model Scenarios

We model bank erosion in the apex reach and distributary channels in two scenarios that contrast a situation without ice with one in which river ice persists in the Staines River distributary channel and the apex, but not in the River Canning distributary channel. This is achieved by tracking the evolution of three separate bank profile positions over 100 years of repeat hydraulic and thermal conditions (Figure 3). We use the 100-year simulation duration to arrive at average rates of erosion without bias in the erosion rate depending on timing of block collapse.

In the first scenario, stage and water temperature are not impacted by river ice (Figure 3, A, C, E, G). In the second scenario, we allow river ice to begin thermal break-up across the delta on May 15th, when air temperature rises above zero, three weeks before discharge peaks during snowmelt (Figure 3, B, D, F, H). We allow ice in the apex transect to take one week to decay, such that τ = 7 days and allow river ice in the Staines River distributary channel to take two weeks to decay, such that τ = 14 days.

We ran 24 exploratory experiments based on unique river ice scenarios, in addition to the ice-free and exemplary scenario of persistent river ice. Specific environmental conditions are generated for the three separate banks by varying t_o relative to the date that discharge begins to rise in the 2009 hydrograph, on June 1st (Figure 2, B). These values are derived from satellite data of river icings on the North Slope of Alaska, including the icings on the Canning River delta (Koch, Best, et al., 2024). We also vary the thermal break-up timescale, τ, or the time it takes for ice to melt by 1/e, representing both ends of a spectrum generated by currently unpredictable values. These simulations are detailed in supplementary material (Table S2).

4.4 Bank Erosion Mapping from Satellite Imagery

We measured bank erosion rates from remote-sensing data (Sentinel L2 imagery, ESA). Higher surfaces bounding the active channel consist of grassy tundra and wetland vegetation, whereas the active channel is frequently reworked and is characterized by sparsely vegetated gravel and sand. Taking advantage of this contrast in surface reflectance properties, we quantify erosion as the lateral distance of vegetated bank line retreat along discrete downstream lengths of bank during 2019-2024.

We used multispectral imagery collected by the European Space Agency's Copernicus Sentinel-2 mission to trace initial and final bank lines (ESA, 2017). Using Google Earth Engine (Gorelick et al., 2017), we selected low-cloud (<10%) images collected in July, August, and September, when vegetation is green, stage is low, and river ice is at its smallest extent. The analysis included five images from 2019 and 10 images from 2024. Before 2019, harmonized data from the Canning River delta are not available.

We calculated reach-wide bank erosion rates as the mean annual distance of bank line retreat over the observation period. The distance of bank line retreat was calculated as the cartesian distance between initial and final bank line positions, which was measured by interpolating points along the initial bank line and calculating their nearest distance to the final bank line. This method assumes that vegetation is not encroaching. It also assumes that bank retreat ensues perpendicular to the initial bank line.

We calculated local permafrost bank erosion rates by isolating the 90^{th} percentile values from the reach-wide analysis rather than the mean. This method assumes that river banks most exposed to thermal erosion will exhibit the fastest erosion rates, whereas some permafrost river banks which are not cemented by ice will have lower erosion rates because they do not undergo collapse due to interstitial ice melt and may be limited by entrainment. We also chose to calculate 90^{th} percentile rates to account for the overestimation of erosion that arises from pixel size and limited observation period. The minimum detectable erosion rate was 2 m/yr, based on pixel size of 10 m, over the 5-year period of observation. We consider measured erosion rates <2 m/yr negligible because they are undifferentiable from no erosion at the resolution of the remote-sensing data.

4. RESULTS

We share field observations from the Canning River delta apex and distributary channel survey sites. These observations inform bank characteristics in the three bank erosion models, each representing a survey site. We explore how fast river banks erode under modern and probable river ice scenarios. Finally, we compare modelled erosion rates to our remote sensing observations.

4.1 Field Observations

Banks have different substrate properties in the apex reach than along distributary channels (Figure 5, Figure S1, Table 2). Near the delta apex, the 2-m high surveyed bank did not exhibit layers of massive ice, but it did contain greater than 50% moisture content by volume. Based on Sentinel Imagery and our own in-situ records, river ice persisted in the channel from October 20, 2021, until open water conditions began on June 15th, 2022. On July 7, 2022, we measured a vertical thaw depth on the upper bank surface of 33 cm. The horizontal distance to the frost table at this time was 23 cm, at 95 cm beneath the bank surface. Soil exposed on this bank is dominated by peat at the top and fine sand-sized fluvial sediments at depth.

The surveyed banks in the Staines River and Canning River distributary channels are characterized by exposed frozen substrate (Figure 4, Figure S1, Table 2). We identified representative stratigraphy within these river bank profiles. The banks are capped by organic-rich topsoil that was thawed in July and August, which is underlain by layers of frozen soil and sediment of up to 98% ice by volume. The Staines River banks had an average of 76% ice by volume, based on a limited number of samples (n=12) taken at different depths along two characteristic bank exposures (Table 2). Frozen substrate on the Staines River bank contains inorganic particles that tend to be fine sand-sized (Figure 4). In early July 2022 at the Staines River survey site, we observed a vertical thaw depth of 29 cm. From 20-175 cm depth in the bank profile, we observed horizontal thaw fronts of 2-8 cm into the bank. The bank profile at the Canning River survey site had visible ice along much of its profile in August of 2021. The Canning River bank contains predominantly silt-sized particles (~50 micron). Some blocks had thawed by July and August, but we also observed blocks on the Staines River bank that were still frozen at their centers.

Along the trunk Canning River and its distributary channels, grain size distributions of fluvial gravel on mid channel bars and bank toes are similar (Arcuri and Overeem, 2025, Table 2). The grain size of fluvial deposits fines slightly downstream, from a D50 of 45 mm at the apex to 23 mm at the Staines River and Canning River distributary channel sites, but permafrost river bank sediment (silt to sand) is always significantly finer than fluvial bed gravel (coarse gravel) (Table 2). Along the trunk Canning River and its distributary channels, grain size distributions of fluvial gravel on mid channel bars and bank toes are similar. The grain size of fluvial deposits fines slightly downstream, but permafrost river bank sediment (silt to sand) is always significantly finer than fluvial bed gravel (coarse gravel) (Table 2). At low flows in June and August, we observed fresh sand deposits on gravel bars.

Bank morphologies in the distributary channels are distinct from those in the apex reach (Table 2, Figure 4). At the apex survey site, the river channel is single thread and hugs the bank on river left, near survey site CR22_Bluff3.

The bank profile is vertical, 2.0 m above fluvial gravel deposits when observed in July of 2023. The Staines River site channel has two threads, with the smaller channel hugging the 1.75 m-tall bank, our survey site CR22_T5. At our survey site on the Canning River distributary channel, CR21_CR2, we measured bank height to be 1.72 m above the water level during collection. Upon sampling in August, collapsed bank sediment had collected on banks, but frozen soil was still visible in places.

The Canning River concentrates into a single channel at the delta apex, where it abuts the left bank and where our survey site is located. The Staines River and Canning River distributary channels exhibit complex planforms which vary between wide, braided channels to anastomosing or wandering ones. All channels exhibit bed slopes of 0.003 m/m, and similar bankfull water depths of 0.6–0.8 m (Table 3).

The three transects exhibit different cross-sectional areas and wetted perimeters (Table 3, Figure S2-3). The Staines River distributary channel has a cross-sectional area that is 76% of the apex channel area. The Canning River distributary channel cross section is 50 and 66% of the apex and Staines River distributary channel cross section size, respectively. In addition, the Staines River distributary channel and apex channels are significantly wider than the Canning River distributary channel.

4.2 Model Predictions

In the apex reach, river ice limits rather than enhances erosion. In the model scenario without river ice, the model predicts that the apex river bank erodes by 1.5 m/year (Table 4, Figure 5). In the persistent icing scenario, where river ice heightens stage and keeps water near freezing during snowmelt, the bank also erodes by 1.5 m/yr. TDD and q_h remain the same between scenarios, but H^* is higher in the modern icing scenario (Table 4, Figure 6). When we compare these scenarios based on A^* and E^*, erosion at the apex site is minimally impacted when ice blocks the channel before the snowmelt peak.

For the Staines River distributary channel, the modern icing scenario results in more bank erosion than the icing-free scenario. The river ice-free scenario results in erosion rates of 3.8 m/yr (Table 4, Figure 5). In the modern icing scenario when the icing thermal break-up period lasts for multiple weeks, the bank erodes at a rate of 4.5 m/yr. In this scenario, A^* is positively correlated to H^* but negatively correlated to TDD (Figure 6). Thus, river icing promotes bank erosion by elevating stage during snowmelt but also inhibits permafrost bank erosion in the Staines River distributary channel by limiting river water temperature during the peak of discharge.

The Canning River distributary channel exhibits faster erosion rates in the modern icing scenario than in the ice-free scenario, like the Staines River

distributary channel. In the absence of river ice blocking the Staines River distributary channel, the banks at the Canning River distributary channel transect are unlikely to erode (Table 4, Figure 5B). However, when the icing in Staines River distributary channel diverts discharge to the Canning River distributary channel during snowmelt, erosion of the Canning River distributary channel bank rises to 2.4 m/yr. E^* for the Canning River distributary channel river bank is positively related to H^* (Table 4, Figure 5). Additionally, erosion in the Canning River distributary channel is weakly related to water temperature and negatively related to heat flux (Figure 6). Here, river ice indirectly increases bank erosion rates by forcing flow into the Canning River distributary channel and extending the duration of bank exposure to river water. In the Canning River distributary channel, the absence of river ice for most of the peak flowenhances the dependency of erosion on the water temperature. The shallow flow heats up rapidly with incoming solar radiation, and river water temperature is not dampened by in-situ icing.

4.3 Comparing Model Predictions to Observations

Based on remote-sensing data, we cannot calculate a bank erosion rate along the entire longitudinal profile due to lack of evidence of consistent active erosion in many sites along either branch. However, individual banks are noticeably eroding in all parts of the delta. In a reach-wide analysis of all three sites, we only measure bank erosion rates of 2-3 m/yr, but up to 10 m/yr at maximum (Figure 5A, Table S1).

At the delta apex, we observed a permafrost bank erosion rate of 1.6 m/yr, up to 3 m/yr (Figure 5A, Table S1). Permafrost bank erosion rates in the Staines River distributary channel are 7.5 m/yr on average but can be as high as 9.3 m locally. This erosion rate is higher than the 6.2 m/yr average rate we observe in the Canning River distributary channel. The highest rate observed locally in the Canning River distributary channel amounts to 9.9 m/yr.

The model scenario without river ice blockages does not reproduce observed permafrost bank erosion rates or regional patterns. Without river ice, the model predicts no erosion in the Canning River distributary channel, unlike our observations (Figure 5A, Table S1). Here, ice-free model underpredicts erosion by 6 m/yr. Additionally, modeled apex bank erosion rates are 1 m/yr slower than we observed. For the Staines River distributary channel bank, the ice-free scenario underpredicts erosion by 3.5 m/yr.

Including river ice in the bank erosion model increases the prediction accuracy of erosion rates and spatial patterns in the distributary channel river banks. With the icing in the Staines River distributary channel, the model still overpredicts erosion at the apex bank by 1 m/yr and at the

Staines River distributary channel bank by 2.5 m/yr. For the Canning River distributary channel, the modern icing scenario produces an erosion rate that is 4 m/yr slower than what we observe. In conclusion, the modern icing scenario predicts erosion rates that are closer to observations.

5. DISCUSSION

Here we discuss some of the limitations of our bank erosion model predictions and the comparison with remote-sensing data.

First, our model oversimplifies hydraulic dynamics. We drive the model with observed discharge over cross-sectional geometries established from Arctic-DEM data analysis. The DEM data do not account for water present in channel threads at time of acquisition, typically low flow, cloud-free days, meaning that all our simulations overestimate stage to a modest amount. This may partially explain overpredictions of erosion rates.

Next, we model river stage while river ice partially fills channels with multiple other assumptions that simplify channel hydraulics. Ice uniformly fills the cross-section, and we do not allow local channelization due to ice. This assumption is appropriate for the Canning River, which is much wider than it is deep, and has little river ice, such that width is relatively stable up to when banks are inundated. However, in the other more ice-dominated branch, local setup of water against banks may be possible during break-up. Therefore, future modeling efforts could incorporate more sophisticated methods for predicting stage and/or velocity from discharge under more complicated ice conditions.

Our modeling approach assumes that thermal erosion is not limited by entrainment of sediment. Previous applications of permafrost bank erosion also account for the delayed entrainment of collapsed bank sediment (Douglas, Dunne and Lamb, 2023; Douglas and Lamb, 2024). For example, on the Koyukuk River in Alaska's discontinuous permafrost zone, erosion transitions from ablation-limited in the early spring to entrainment-limited in the summer due to excess collapsed sediment on river banks that disconnects river water from the bank frost table (Rowland et al., 2023; Douglas and Lamb, 2024; Geyman et al., 2024). Here, river banks erode by 2 to 6 m/yr (Geyman et al., 2024). Unlike in the Koyukuk River, collapsed bank sediment is much finer than bed load in the Canning River; therefore, collapsed bank sediment is easily entrained when stage is high enough to inundate ice-rich substrate. We observed thermal erosion with blocks present and block entrainment in the flow during all our field visits over several summers (2021-2024). Therefore, entrainment is unlikely to limit bank erosion in the distributary channels for the fine-grained Alaska Arctic Coastal Plain setting.

The bank erosion retrieved from remote-sensing data is appropriate for characterizing relative permafrost bank erosion rates under different river ice conditions but is limited in accuracy. Remote sensing data analysis detects permafrost bank erosion at up to 10 m/yr within the range of previously published values of 1-10 m/yr on average (Costard et al., 2003; Rowland et al., 2023), and up to 40 meters of erosion in a year. However, reach-averaged rates are less than or equal to the minimum detectable erosion rate based on Sentinel data resolution (10-m resolution and a 5-year record). Therefore, we cannot precisely resolve the long-term changes in width that the Canning River delta distributary channels experience. Thus, bank erosion in this setting varies highly both locally and from year-to-year.

Our model is applicable to permafrost rivers in in the Alaska Arctic Coastal Plain but might not apply to all permafrost rivers. On the Koyukuk River in Interior Alaska, permafrost banks erode by 3 m/yr, on average (Geyman et al. 2024). Still, the Koyukuk River is in discontinuous permafrost and has coarser bank sediment and lower ice content, such that river bank erosion in this setting is less likely to be entirely driven by thermal erosion and will experience more effects from entrainment limiting erosion (Geyman et al., 2024; Douglas, Dunne, and Lamb, 2023). In the Lena River in Arctic Russia, where permafrost soils can be ice-rich, individual banks eroded by 2 to 40 m/yr between 2009 and 2012 (Costard et al., 2014). At ~3 km wide, the Lena River is much larger than most Arctic rivers, and its banks are comprised of material that is 20-40% ice. The Lena River channel ices over, but as in most large Arctic rivers, there is substantial under-ice water discharge even during winter. This means that blockages of river ice will develop in a different manner. Therefore, our model is most applicable to smaller Arctic rivers that can develop substantial bedfast icings, and that can easily entrain fine bank material when banks are inundated.

Our findings demonstrate how river icings can exert a dominant control on permafrost river bank erosion in a delta. Without any river icing, like in full summer conditions, erosion rates scale positively with water temperature, exposure to river water, and river water heat flux (Costard et al., 2003; Dupeyrat et al., 2011). Icings in deltas can complicate this scaling by altering channel geometry and water temperature in the larger, icing-occupied channel and activating smaller, low-flow distributary channels during snowmelt.

We argue that there may even be some predictability to these dynamics, especially in delta distributary channels (Figure 7). Winter river ice may accumulate most easily in the channel that carried most flow in late fall. That channel will have the most seeping water through winter due to an unfrozen channel bed, or Talik. When ice persists in this otherwise largest distributary channel through snowmelt, river banks in this channel tend to

be exposed to deeper and much cooler water during the highest stage in spring. Thus, banks in this part of the delta system are only exposed to warmer water at lower stage in summer after river ice has decayed (Figure 1, Figure 7 A-C).

Conversely, the channel with limited flow during the fall season accumulates less ice over winter. As in our example system, erosion in the Canning River distributary channel is highest while ice persists in Staines River distributary channel through spring and early summer. When ice blocks the Staines River distributary channel, water is diverted into the Canning River distributary channel, causing rapid erosion during the early and only part of the flow season that the frozen bank is exposed to river water (Table 4, Figure 7D-F). Because the Canning channel has little river ice, the water entering it can more rapidly warm from incoming radiation.

What does the model imply for the future, in which the icing is more – or less – resistant to thermal break-up? We address this question by comparing modeled erosion rates in our additional scenarios based on the start and duration of the river ice break-up period (Figure 8). We find that bank erosion rates are highest in distributary channels when thermal break-up of the icing coincides with the snowmelt peak, in the first week of June. Alternatively, permafrost bank erosion rates are concentrated in the icing-impacted channel in years when the icing is less resistant to thermal break-up. The delta apex river bank is unlikely to be influenced by the duration of thermal break-up because all model scenarios produce roughly equal erosion rates.

These future model scenarios indicate that river ice plays a role in delta channel morphologies by filling the largest distributary channel and activating small, otherwise low-flow distributary channels in spring. Permafrost on river corridor boundaries that is not accessed by late-season flow is therefore most susceptible to erosion in years when an icing in the delta is especially resistant to break-up. In years when summer storms are more frequent or summer discharge is relatively high, the largest distributary channel could experience faster erosion rates than we have predicted. Additionally, changes to the duration of thermal break-up due to thicker, or thinner, river icings could impact distributary channel morphologies and the configurations of deltas in the Arctic Coastal Plain.

6. CONCLUSION

Results of our numerical modeling study show that permafrost river bank erosion in small Arctic deltas is sensitive to both the thermal and hydraulic impacts of river ice. Wide distributary channels that receive the most flow in summer and fall develop the most river icing over winter. This river ice tends to divert early flow away, even if it also elevates local stage. The river ice

remains for several weeks and cools river water to reduce predicted bank erosion. For our specific case-study in the Canning River delta, this situation is documented in the Staines River distributary channel (Fig. 5). On these wide, dominant distributary channels with icings, our models predict that future bank erosion increases more rapidly when the icing completes thermal break-up before snowmelt. In a warmer future, any blockage and cooling effects of river ice disappear (Figure 8). For permafrost banks in less-frequently occupied distributary channels that tend receive less flow in summer, erosion rates are highest when river ice diverts water from the main channel into that specific distributary during snowmelt. In this ice-free part of the network, water will warm up more rapidly with solar radiation, whereas water remains freezing in the part of the channel network with recurrent icings. The Canning River distributary channel exemplifies this scenario, and our predictions show that little erosion would occur in these more quiescent distributaries if no ice were present (Fig 5B).

The spatiotemporal erosion dynamics result from the nonlinear relationship between river stage, water temperature, and fluvial heat transfer when river ice unevenly occupies distributary channels. Comparing modeled erosion rates among all scenarios suggests that full inclusion of thermal processes should improve our ability to predict river bank erosion in permafrost terrain.

Arctic rivers will likely continue adjusting to warming, but system-specific responses are muddied by river ice processes. Rivers are expected to receive more water, experience fewer snow-covered days, and continued warming of permafrost at depth (Magnuson et al., 2000; Yang et al., 2020; Feng et al., 2021; Smith et al., 2022). In Arctic deltas, some river icings grow thicker over winter and persist further into summer, while decreasing in annual extent elsewhere. Our results suggest that bank erosion rates across deltas with icings depend on when river ice begins to melt relative to arrival of the snowmelt and how long the thermal break-up period lasts, which both control ice thickness through spring (Fig 8). Considering the thermal and hydraulic effects of river ice could improve models for permafrost river dynamics, with implications for mobilization of permafrost soil carbon and sediment delivery to the Arctic Ocean.

REFERENCES

Anderson, S. Cochran. C., Anderson, R.S., Repasch, M., Arcuri, J., and Overeem, I. (2024) 'A conceptual carbon budget for an icy riverine corridor', in *ICOP 2024 12th International Conference on Permafrost. Whitehorse, Yukon, Canada: 16–20 June, 2024*. Available from: https://doi.org/https://doi.org/10.52381/ICOP2024.161.1.

Barnhart, K.R., Anderson, R.S., Overeem, I., Wobus, C., Clow, G.D. and Urban, F. (2013) 'Modeling erosion of ice-rich permafrost bluffs along the

789 Alaskan Beaufort Sea coast', *Journal of Geophysical Research F: Earth*
790 *Surface*, 119(5), pp. 1155–1179. Available from:
791 https://doi.org/10.1002/2013JF002845.

792 Best, H., McNamara, J. P. and Liberty, L. (2005) 'Association of Ice and River
793 Channel Morphology Determined Using Ground-penetrating Radar in the
794 Kuparuk River, Alaska', Arctic, Antarctic, and Alpine Research, 37(2), pp.
795 157–162. Available from: 10.1657/1523-
796 0430(2005)037[0157:AOIARC]2.0.CO;2.

797 Biskaborn, B.K., Smith, S.L., Noetzli, J., Matthes, H., Vieira, G., Streletskiy,
798 D.A., Schoeneich, Romanovsky, V.E., Lewkowicz, A.G., Abramov, A., Allard,
799 M., Boike, J., Cable, W.L, Christiansen, H.H., Delaloye, R., Diekmann, B.,
800 Drozdov, D., Etzelmüller, B., Grosse, G., Guglielmin, M., Ingeman-Nielsen,
801 T., Isaksen, K., Ishikawa, M., Johansson, M., Johannsson, H., Joo, A.,
802 Kaverin, D., Kholodov, A., Konstantinov, P., Kröger, T., Lambiel, C.,
803 Lanckman, J, Luo, D., Malkova, G., Meiklejohn, I., Moskalenko, N., Olina, M.,
804 Phillips, M., Ramos, M., Sannel, A.B.K., Sergeev, D., Seybold, C., Skybrin,
805 P., Vasiliev, A., Wu, Q., Yoshikawa, K., Zheleznyak, M. and Lantuit, L.
806 (2019) 'Permafrost is warming at a global scale', *Nature Communications*,
807 10(1), pp. 1–11. Available from: https://doi.org/10.1038/S41467-018-
808 08240-4.

809 Blaskey, D., Koch, J.C., Gooseff, M.N., Newman, A.J., Cheng, Y., O'Donnell,
810 J.A. and Musselman, K.N. (2023) 'Increasing Alaskan river discharge during
811 the cold season is driven by recent warming', *Environmental Research*
812 *Letters*, 18(2). Available from: https://doi.org/10.1088/1748-9326/ACB661.

813 Box, J.E., Colgan., W.T., Christensen, T.R., Schmidt, N.M., Lund, M.,
814 Parmentier, F.W., Brown, R., Bhatt, U.S., Euskirchen, E., Romanovsky, V.E.,
815 Walsh, J.E., Overland, J.E., Wang, M., Corell, R.W., Meier, W.N., Wouters,
816 B., Mernild, S., Mård, J., Pawlak, J. and Olsen, M.S. (2019) 'Key indicators of
817 Arctic climate change: 1971–2017', *Environmental Research Letters*, 14(4),
818 p. 045010. Available from: https://doi.org/10.1088/1748-9326/AAFC1B.

819 Briner, Jason P., and Darrell S. Kaufman. "Late Pleistocene mountain
820 glaciation in Alaska: key chronologies." *Journal of Quaternary Science:*
821 *Published for the Quaternary Research Association* 23, no. 6-7 (2008): 659-
822 670. Available from: https://doi.org/10.1002/jqs.1196

823 Bunte, K. and Abt, S.R. (2001) 'Sampling surface and subsurface particle-
824 size distributions in wadable gravel-and cobble-bed streams for analyses in
825 sediment transport, hydraulics, and streambed monitoring', *Gen. Tech. Rep.*
826 *RMRS-GTR-74. Fort Collins,CO: U.S. Department of Agriculture, Forest*

Service, Rocky Mountain Research Station. 428 p., 74. Available from: https://doi.org/10.2737/RMRS-GTR-74.

Burrell, B.C., Beltaos, S. and Turcotte, B. (2023) 'Effects of climate change on river-ice processes and ice jams', *International Journal of River Basin Management*, 21(3), pp. 421–441. Available from: https://doi.org/10.1080/15715124.2021.2007936.

Chassiot, L., Lajeunesse, P. and Bernier, J.F. (2020) 'Riverbank erosion in cold environments: Review and outlook', *Earth-Science Reviews*, 207, p. 103231. Available at: https://doi.org/10.1016/J.EARSCIREV.2020.103231.

Coon, W.F. (1998) *Estimation of roughness coefficients for natural stream channels with vegetated banks* (Vol. 2441). US Geological Survey. Available from: https://doi.org/10.3133/wsp2441

Costard, F., Dupeyrat, L., Gautier, E. and Carey-Gailhardis, E., 2003. 'Fluvial thermal erosion investigations along a rapidly eroding river bank: application to the Lena River (central Siberia)'. *Earth Surface Processes and Landforms*, 28(12), pp.1349-1359. Available from: https://doi.org/10.1002/esp.592.

Costard F., Gautier E., Fedorov A., Konstantinov P. and Dupeyrat L. (2014), An Assessment of the Erosion Potential of the Fluvial Thermal Process during Ice Breakups of the Lena River (Siberia), Permafrost and Periglacial Processes, 25, pages 162–171, Available from: 10.1002/ppp.1812.

Douglas, M.M., Dunne, K.B.J. and Lamb, M.P. (2023) 'Sediment Entrainment and Slump Blocks Limit Permafrost Riverbank Erosion', *Geophysical Research Letters*, 50(11), p. e2023GL102974. Available from: https://doi.org/10.1029/2023GL102974.

Douglas, M.M. and Lamb, M.P. (2024) 'A Model for Thaw and Erosion of Permafrost Riverbanks', *Journal of Geophysical Research: Earth Surface*, 129(4), p. e2023JF007452. Available from: https://doi.org/10.1029/2023jf007098.

Dupeyrat, L., Costard, F., Randriamazaoro, R., Gailhardis, E., Gautier, E. and Federoz, A. (2011) 'Effects of ice content on the thermal erosion of permafrost: Implications for coastal and fluvial erosion', *Permafrost and Periglacial Processes*, 22(2), pp. 179–187. Available at: https://doi.org/10.1002/PPP.722.

Ensom, T., Makarieva, O., Morse, P., Kane, D., Aleskeev, V., Marsh, P. (2020) 'The distribution and dynamics of aufeis in permafrost regions',

Permafrost and Periglacial Processes, 31(3), pp. 383–395. Available from: https://doi.org/10.1002/ppp.2051.

Ettema, R. (2002) 'Review of alluvial-channel responses to river ice', *Journal of Cold Regions Engineering*, 16(4), pp.191-217. Available from: https://doi.org/10.1061/(ASCE)0887-381X(2002)16:4(191)

European Space Agency, 2017, Harmonized Sentinel-2 MSI: MultiSpectral Instrument, Level-2A (SR), accessed January 2024, at https://developers.google.com/earth-engine/datasets/catalog/sentinel.

Ferguson, R. (2007), Flow resistance equations for gravel- and boulder-bed streams, Water Resour. Res., 43, W05427, Available from:10.1029/2006WR005422.

Feng, D., Gleason, C.J., Lin, P., Yang, X., Pan, M. and Ishitsuka, Y. (2021) 'Recent changes to Arctic river discharge', *Nature communications*, *12*(1), p.6917. Available from: https://doi.org/10.1038/s41467-021-27228-1.

Fields, J., Kreisler, J., Dethier, E., Perrotti, J. and Renshaw, C. (2025) 'Fluvial erosion linked to warming in the Canadian Arctic', *Communications Earth & Environment,* 6(1), p.267. Available from: https://doi.org/10.1038/s43247-025-02234-z.

Geyman, E.C. Douglas, M.M., Avouac, J., Lamb, M.P.(2024) 'Permafrost slows Arctic riverbank erosion', *Nature*, 634(8033), pp. 359–365. Available at: https://doi.org/10.1038/S41586-024-07978-W.

Gorelick, N., Hancher, M., Dixon, M., Ilyushchenko, S., Thau, D. and Moore, R. (2017) 'Google Earth Engine: Planetary-scale geospatial analysis for everyone', *Remote Sensing of Environment*, 202, pp. 18–27. Available from: https://doi.org/10.1016/J.RSE.2017.06.031.

Harris, S.A., French, H.M., Heginbottom, J.A., Johnston, G.H., Ladanyi, B., Sego, D.C. and van Everdingen, R.O. (1988) *Glossary of Permafrost and Related Ground-Ice Terms*, *National Research Council of Canada Technical Memorandum*. Available from: https://www.permafrost.org/wp-content/uploads/Glossary/Glossary_of_Permafrost_and_Related_Ground-Ice_Terms_1998.pdf (Accessed: 4 June 2025).

Hoque, M.A. and Pollard, W.H. (2016) 'Stability of permafrost dominated coastal cliffs in the Arctic', *Polar Science*, 10(1), pp. 79–88. Available from: https://doi.org/10.1016/J.POLAR.2015.10.004.

Ielpi, A., Lapôtre, M.G.A., Finotello, A. and Roy-Léveillée, P.(2023) 'Large sinuous rivers are slowing down in a warming Arctic', *Nature Climate*

Change, 13(4), pp. 375–381. Available from: https://doi.org/10.1038/S41558-023-01620-9.

Intergovernmental Panel on Climate Change [IPCC] (2023) 'Climate Change 2023: Synthesis Report, Summary for Policymakers. Contribution of Working Groups I, II and III to the Sixth Assessment Report of the Intergovernmental Panel on Climate Change'. Available from: https://doi.org/10.59327/IPCC/AR6-9789291691647.001.

Kane, D.L., Hinzman, L.D., McNamara, J.P., Zhang, Z., Benson, C.S. (2000) 'An Overview of a Nested Watershed Study in Arctic Alaska: Paper presented at the 12th Northern Res. Basins/Workshop (Reykjavik, Iceland – Aug.23rd - 27th 1999)', *Hydrology Research*, 31(4–5), pp. 245–266. Available from: https://doi.org/10.2166/nh.2000.0015.

Kanevskiy, M., Shur, Y. and Jorgenson, T. (2018) 'Ice-wedge thermokarst: Past, present, and future', In *5th European Conference On Permafrost–Book of Abstracts, 23 June–1 July 2018, Chamonix, France*. Available from: https://par.nsf.gov/biblio/10110430.

Koch, J.C., Best, H., Baughman, C., Couvillion, C., Carey, M.P. and Conaway, J. (2024) *A comparison of contemporary and historical hydrology and water quality in the foothills and coastal plain of the Arctic National Wildlife Refuge, Arctic Slope, northern Alaska*, *Scientific Investigations Report*. Reston, VA. Available from: https://doi.org/10.3133/sir20245008.

Koch, J.C., Connolly, C.T., Connolly, C.T., Bauighman, C., Repasch, M., Best, H. and Hunt, A. (2024) 'The dominance and growth of shallow groundwater resources in continuous permafrost environments', *Proceedings of the National Academy of Sciences*, 121(23), p. e2317873121. Available from: https://doi.org/10.1073/pnas.2317873121.

Kokelj, S. V and Jorgenson, M.T. (2013) 'Advances in Thermokarst Research', *Permafrost and Periglacial Processes*, 24(2), pp. 108–119. Available from: https://doi.org/10.1002/ppp.1779.

Lachenbruch, A.H. and Marshall, B.V. (1986) 'Changing Climate: Geothermal Evidence from Permafrost in the Alaskan Arctic', *Science*, 234(4777), pp. 689–696. Available from: https://doi.org/10.1126/science.234.4777.689.

Magnuson, J.J., Robertson, D.M., Benson, B.J., Wynne, R.H., Livingstone, D.M., Arai, T., Assel, R.A., Barry, R.G., Card, V., Kuusisto, E., Granin, N.G., Prowse, T.D., Stewart, K.M. and Vuglinski, V.S. (2000) 'Historical trends in lake and river ice cover in the Northern Hemisphere', *Science*, 289(5485),

pp. 1743–1746. Available from: https://doi.org/10.1126/SCIENCE.289.5485.1743.

Marsh, P. and Prowse, T.D. (1987) 'Water temperature and heat flux at the base of river ice covers', *Cold Regions Science and Technology*, 14(1), pp. 33–50. Available from: https://doi.org/10.1016/0165-232X(87)90042-5.

Overeem, I., Nienhuis, J.H. and Piliouras, A. (2022) 'Ice-dominated Arctic deltas', *Nature Reviews Earth & Environment 2022 3:4*, 3(4), pp. 225–240. Available from: https://doi.org/10.1038/s43017-022-00268-x.

Parker, G. (1991) 'Selective sorting and abrasion of river gravel. II: Applications', *Journal of Hydraulic Engineering*, 117(2), 150–171, Available from: https://doi.org/10.1061/(ASCE)0733-9429(1991)117:2(150).

Porter, C., Morin, P., Howat, I., Noh, M., Bates, B., Peterman, K., Keesey, S., Schlenk, M., Gardiner, J., Tomko, K., Willis, M., Kelleher, C., Cloutier, M., Husby, E., Foga, S., Nakamura, H., Platson, M., Wethington, M., Williamson, C., Bauer, G., Enos, J., Arnold, G., Kramer, W., Becker, P., Doshi, A., D'Souza, C., Cummens, P., Laurier, F. and Bojesen, M. (2023). 'ArcticDEM, Version 4.1'. Available from: https://doi.org/10.7910/DVN/3VDC4W, Harvard Dataverse, V1, [accessed January 2024]

Prowse, T.D. and Beltaos, S. (2002) 'Climatic control of river-ice hydrology: A review', *Hydrological Processes*, 16(4), pp. 805–822. Available from: https://doi.org/10.1002/HYP.369.

Randriamazaoro, R., Dupeyrat, L., Costard, F., Gailhardis, E.C. (2007) 'Fluvial thermal erosion: Heat balance integral method', *Earth Surface Processes and Landforms*, 32(12), pp. 1828–1840. Available from: https://doi.org/10.1002/ESP.1489.

Ravens, T.M. and Peterson, S. (2021) 'Geologic Controls on Erosion Mechanism on the Alaska Beaufort Coast', *Frontiers in Earth Science*, 9, p. 693824. Available from: https://doi.org/10.3389/FEART.2021.693824/BIBTEX.

Romanovsky, V.E., Smith, S.L. and Christiansen, H.H. (2010) 'Permafrost thermal state in the polar northern hemisphere during the international polar year 2007-2009: A synthesis', *Permafrost and Periglacial Processes*, 21(2), pp. 106–116. Available from: https://doi.org/10.1002/PPP.689.

Rowland, J.C., Schwenk, J.P., Shelef, E., Muss, J., Ahrens, D., Stauffer, S., Pilliouras, A., Crosby, B., Chadwick, A., Douglas, M., M., Kemeny, P.C., Lamb, M. P., Li, G.K. and Vulis, L. (2023) 'Scale-Dependent Influence of

Permafrost on Riverbank Erosion Rates', *Journal of Geophysical Research: Earth Surface*, 128(7), p. e2023JF007101. Available from: https://doi.org/10.1029/2023JF007101.

Smith, S.L., O'Neill, H.B., Isaksen, K., Noetzli, J. and Romanovsky V.E. (2022) 'The changing thermal state of permafrost', *Nature Reviews Earth & Environment 2022 3:1*, 3(1), pp. 10–23. Available from: https://doi.org/10.1038/s43017-021-00240-1.

Tananaev, N. I. (2016) 'Hydrological and sedimentary controls over fluvial thermal erosion, the Lena River, central Yakutia', *Geomorphology*, 253, 524-533.Available from: https://doi.org/10.1016/j.geomorph.2015.11.009.

Tananaev, N. and Lotsari, E. (2022) 'Defrosting northern catchments: Fluvial effects of permafrost degradation', *Earth-Science Reviews*, 228, p. 103996. Available from: https://doi.org/10.1016/j.earscirev.2022.103996.

Turcotte, B. and Morse, B. (2013) 'A global river ice classification model', *Journal of Hydrology*, 507, pp. 134–148. Available from: https://doi.org/10.1016/J.JHYDROL.2013.10.032.

Turetsky, M.R. Abbot, B.W., Jones, M.C., Anthony, K.W., Olefeldt, D., Schuur, E.A.G., Grosse, G., Kuhry, P., Hugelius, G., Koven, C.,Lawrence, D.M., Gibson, C., Sannel, A.B. and McGuire, A.D. (2020) 'Carbon release through abrupt permafrost thaw', *Nature Geoscience*, 13(2), pp. 138–143. Available from: https://doi.org/10.1038/S41561-019-0526-0.

U.S. Geological Survey (2023). USGS water data for the Nation. *US Geological Survey National Water Information System database*. Accessed June 30, 2023, at https://doi.org/10.5066/F7P55KJN.

Walker, H.J. and Hudson, P.F. (2003) 'Hydrologic and geomorphic processes in the Colville River delta, Alaska', *Geomorphology*, 56(3–4), pp. 291–303. Available from: https://doi.org/10.1016/S0169-555X(03)00157-0.

Webb, B.W. and Zhang, Y. (1997) 'spatial and seasonal variability in the components of the river heat budget', *Hydrological Processes*, 11(1), pp. 79–101. Available from: https://doi.org/10.1002/(SICI)1099-1085(199701)11:1.

Wilson, F., Hults, C., Mull, C. and Karl, S. (2015) 'Geologic map of Alaska', USGS Publications Warehouse, Available from: https://doi.org/10.3133/SIM3340.

Wohl, E. and Scamardo, J.E. (2022) 'Aufeis as a Major Forcing Mechanism for Channel Avulsion and Implications of Warming Climate', *Geophysical*

Research Letters, 49(20), p. e2022GL100246. Available from: https://doi.org/10.1029/2022GL100246.

Wolman, M.G. (1954) 'A method of sampling coarse river-bed material', *Eos, Transactions American Geophysical Union*, 35(6), pp. 951–956. Available from: https://doi.org/10.1029/TR035I006P00951.

Xie, P. and Arkin, P.A. (1997) 'Global precipitation: A 17-year monthly analysis based on gauge observations, satellite estimates, and numerical model outputs'*, Bulletin of the American Meteorological Society,* 78(11), pp.2539-2558, Available from: https://doi.org/10.1175/1520-0477(1997)078<2539:GPAYMA>2.0.CO;2.

Yang, X., Pavelsky, T.M. and Allen, G.H. (2020) 'The past and future of global river ice', *Nature*, 577(7788), pp. 69–73. Available from: https://doi.org/10.1038/S41586-019-1848-1.

Zheng, L., Overeem, I., Wang, K. and Clow, G.D. (2019). Changing Arctic river dynamics cause localized permafrost thaw. *Journal of Geophysical Research: Earth Surface*, 124(9), pp.2324-2344. Available from: https://doi.org/10.1029/2019JF005060

TABLES

Table 1: List of bank erosion model parameters

Parameter	Value	Units	Description	Source
Bank Properties				
T_{pf}	-8.0	°C	Permafrost temperature	Canning River Meteorological Station
ρ_s	2650	kg/m^3	Bank sediment density	Barnhart et al. (2013)
c_p	1,350	J/kg/°C	Permafrost heat capacity	Barnhart et al. (2013)
Ablation				
k_s	-	m	Grain roughness length scale	-
T_0	0	°C	Bulk water freezing temperature	Costard et al. (2003)
L_i	335,000	J/kg	Latent heat of ice	Costard et al. (2003)
ρ_i	917	kg/m3	Ice density	Costard et al. (2003)
k_b	2.30	m /°C	River bed thermal conductivity	Barnhart et al. (2013)
k_w	0.6	m /°C	River water thermal conductivity	Costard et al. (2003)
ν_w	1.5 x 10^{-6}	m^2 /s	River water kinematic viscosity at 10˚C	Costard et al. (2003)
μ	1.3 x 10^{-3}	Pa s	River water dynamic viscosity at 10˚C	Costard et al. (2003)
C_f	-	-	Friction coefficient	-
$c_{p,w}$	4210	J/kg /°C	River water heat capacity	Costard et al. (2003)
C_h	-	m/s	Fluvial heat transfer coefficient	-
Collapse				
d_{iw}	-	m	Ice wedge depth	-
τ_{pf}	200	kPa	Permafrost tensile strength	Costard et al. (2003)
River Ice and Hydraulic Dynamics				
A_i	-	m^2	River ice cross sectional area	-
U^*	-	-	Shear velocity	-
R	0.2	-	Water surface albedo	Zheng et al. (2019)
f	0.05	-	Attenuation coefficient	Zheng et al. (2019)
a	0.6	-	Fraction of radiation absorbed by water	Zheng et al. (2019)
b	0.2	-	Fraction of radiation absorbed by river bed	Zheng et al. (2019)
His	-	W/m^2	Incident shortwave radiation	Canning River Meteorological Station

Hl	-	W/m^2	net surface longwave radiation	
Hc	-	W/m^2	Convective hear flux	
Hsr	-	W/m^2	net surface shortwave radiation	
Hb	-	W/m^2	River bed heat flux	
T_w	-	°C	River water temperature	-
H	-	m	River water depth	-
Q	-	m^3/s	River water discharge	-
t_f	October 1st	days	Day river ice starts to accumulate	Canning River Meteorological Station
t_o	-	days	Day river ice thermal break-up begins	Canning River Meteorological Station
τ	-	days	River ice thermal break-up timescale	-
n_c	.05	-	Composite manning's roughness coefficient	Coon (1998)
C_f	-	-	Bed friction coefficient	-
Spacing and timing				
t	-	s	Time since simulation start	-
z	-	m	Vertical distance from base of bank	-
x	-	m	Horizontal distance from starting position	-
x_o	-	m	Notch horizontal position	-
z_o	-	m	Notch vertical position	-
x_{iw}	-	m	Ice wedge center horizontal position	-
dt	3	hours	Time step	-
dz	1	cm	Vertical spacing on bank profile	-

1026

1027 Table 2: Survey site bank properties

River bank location		Delta apex	Staines River distributary channel	Canning River distributary channel
Frozen ground volumetric ice content (%)	f_i	50	80	*Not measured*
Depth-averaged median inorganic particle diameter (microns)	$D50_{bank}$	100	50	50
Number of sampled layers	-	4	3	3
50th percentile diameter of channel bed gravel (mm)	$D50_{bed}$	45	23	23
84th percentile diameter of channel bed (mm)	$D84_{bed}$	91	64	64
Bank surface height above fluvial gravel (m)	h_b	2.00	1.75	1.72
Fluvial gravel height above channel bed (m)	z_g	0.8	0.5	0.3
Ice wedge polygon trough spacing (m)	Δx_w	4	35	35

1028

1029 Table 3: Channel cross-sectional geometry

	Delta apex	Staines River distributary channel	Canning River distributary channel
Bankfull Width (m)	800	800	500
Bankfull Wetted Perimeter (m)	840	790	450
Bankfull Mean Water Depth (m)	0.83	0.63	0.66
Bankfull Hydraulic Radius (m)	0.80	0.63	0.73
Width-to-depth ratio (m:m)	1100:1	1300:1	600:1
Bankfull wetted area (m^2)	670	500	330

1030

1031 Table 4: Model Results

Scenario	Survey Site	E (m/yr)	E^*	A^*	H^*	TDD (°C days)	q_h (J/m^2)

		River bank erosion rate	Mean annual river bank erosion	Mean annual channel blockage by ice	Mean annual bank exposure to water	Annual river water thawing degree days	Cumulative river water heat flux
no river ice	Apex	1.5	0.002	0.000	0.064	1362	14E+09
	Staines	3.8	0.005	0.000	0.097	1354	9.6E+09
	Canning	0.0	0.000	0.000	0.000	1349	0.0
modern river icing	Apex	1.5	0.002	0.195	0.073	1362	14E+09
	Staines	5.6	0.007	0.428	0.142	1241	8.5E+09
	Canning	2.5	0.005	0.000	0.037	1351	22E+09

1032

1033

FIGURE CAPTIONS

Figure 1: A: The Canning River's location in Northeastern Alaska, including geographic landmarks and major rivers (USGS, 2023), and surface elevations from ArcticDEM (Porter et al., 2023). B–D: cloud-free composite images using Sentinel 2-L2A True Color satellite images from 2023 B: April – May 15th composite, C: May 15th -June 15th composite, and D: July-August composite. E: Schematic legend of the Canning River delta and the locations of field surveys.

Figure 2: A: Daily mean air temperature record from the Canning River Meteorological Station (Frank Urban, unpublished data, 2023). B: Daily mean discharge record from USGS station 15955000 during 2008–2010 (USGS, 2023).

Figure 3: Environmental conditions for the three channels in the no ice scenario (A, C, E, G) and the modern icing scenario (B, D, F, H). A and B: River ice cross sectional area for the scenario without ice and the modern icing scenario, respectively. C and D: River discharge. E and F: Hydraulic radius. G and H: River water temperature, and the grey line in the background shows the daily mean air temperature recorded by the USGS Canning River Meteorological Station (Frank Urban, unpublished data, 2023).

Figure 4: Photographs of characteristic river banks at the delta apex (A and C) and the Staines River distributary channel (B and D). Labels indicate stratigraphic features and examples of field measurements. Photograph credit: M. Repasch.

Figure 5: Measured permafrost bank erosion rates and modeled erosion rates from all model simulations. A. Bnk erosion measurements displayed by site. Error bars are located at the 10th and 90th percentiles. B. erosion rates from all model scenarios in violin plots, and results from the no river ice scenario (cross marker) and the exemplary modern thermal break-up scenario(filled circle).

Figure 6: Comparison of model result based on metrics: A. Mean annual river ice blockage (A*) for all model scenarios. B. Mean annual river bank exposure (H*). C. River water Thawing Degree-Days (TDD). D. cumulative river water heat flux (q_h).

F

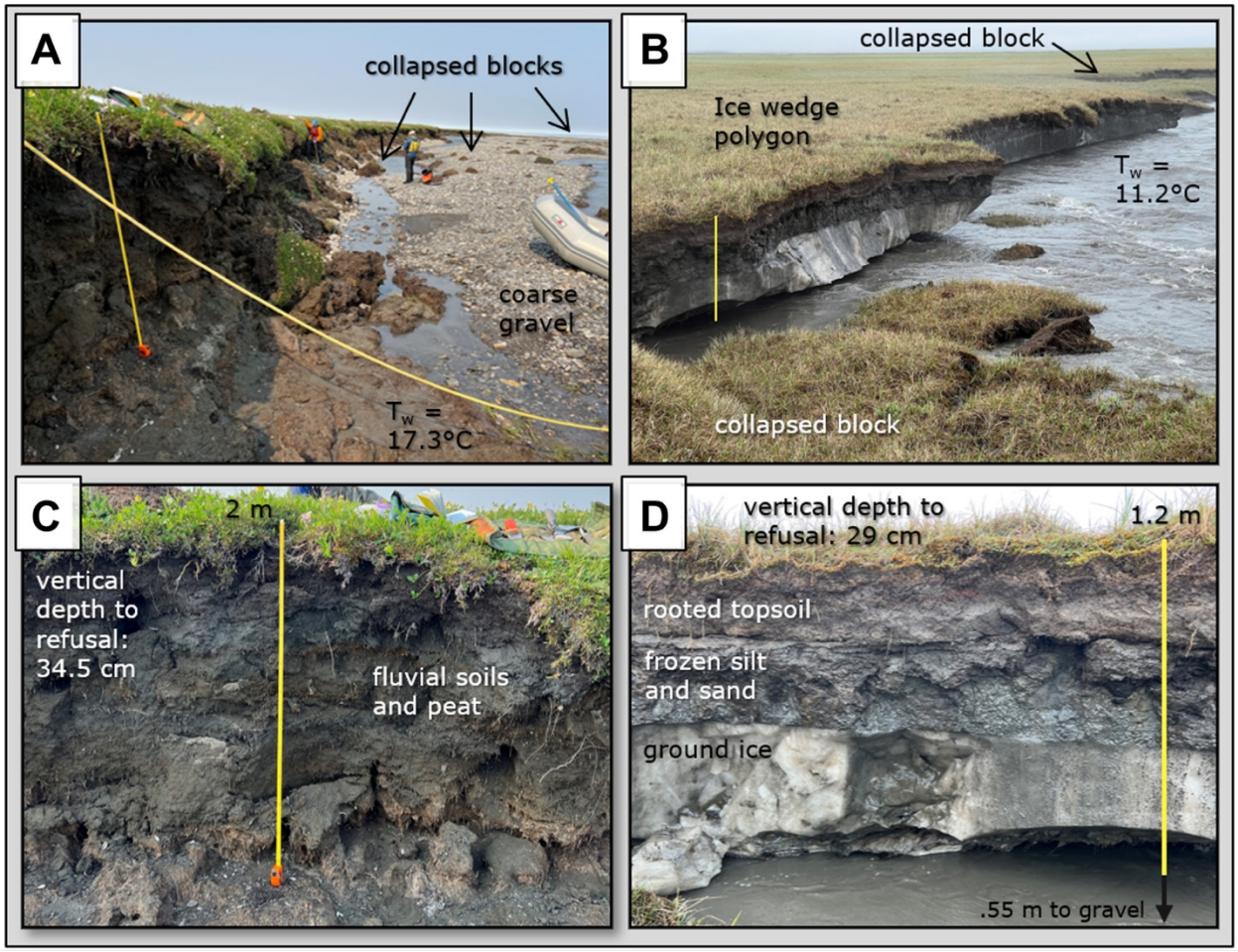

igure 7. A conceptual model for permafrost river bank erosion in an Arctic delta where river ice resists break-up in spring. A: in a large distributary channel, river ice impacts thermal erosion by cooling water but increasing bank exposure to water. White triangles display bedfast river ice conditions during the thermal break-up period. B: following ice break-up, warm river water from summer storms undercuts river banks. C: Undercutting from late-season thermal erosion generates an overhanging block. D: In a smaller distributary channel that does not fill with ice over winter, thermal erosion undercuts banks when they are inundated in spring. E: although banks are infrequently exposed to water in summer, undercutting triggers an upper bank collapse, as the driving torque exceeds the resisting torque. F: banks are relatively stable in fall because thermal erosion is unlikely. Refer to Table 1 for parameters definitions.

Figure 8: Relative bank erosion rates for the Staines River and Canning River distributary channel river banks from all model scenarios as a function of the duration of thermal break-up of the icing in the Staines River distributary

channel. Bank erosion rates for the apex site are plotted against the local thermal break-up duration rather than the thermal break-up duration of the icing in the Staines River distributary channel.